

On the specific energy and pressure in near-Earth magnetic clouds

Debesh Bhattacharjee¹ Prasad Subramanian¹ Angelos Vourlidas² Teresa Nieves-Chinchilla³ Niranjana Thejaswi⁴ and Nishtha Sachdeva⁵

¹ Indian Institute of Science Education and Research, Pune Dr. Homi Bhabha Road, Pashan, Pune 411008, India

² The Johns Hopkins University Applied Physics Laboratory, Laurel MD, USA.

³ Heliophysics science division, NASA-Goddard Space Flight Center, Greenbelt, MD (USA).

⁴ Department of Physics, The University of Arizona, Tucson, AZ 85721, USA

⁵ Department of Climate and Space Science and Engineering, University of Michigan, Ann Arbor, USA

November 1, 2022

ABSTRACT

Context. The pressure and energy density of the gas and magnetic field inside solar coronal mass ejections (in relation to that in the ambient solar wind) is thought to play an important role in determining their dynamics as they propagate through the heliosphere.

Aims. We compare the specific energy (erg g^{-1}) [comprising kinetic (H_k), thermal (H_{th}) and magnetic (H_{mag}) contributions] inside MCs and the solar wind background. We examine if the excess thermal + magnetic pressure and specific energy inside MCs (relative to the background) is correlated with their propagation and internal expansion speeds. We ask if the excess thermal + magnetic specific energy inside MCs might make them resemble rigid bodies in the context of aerodynamic drag.

Methods. We use near-Earth *in-situ* data from the WIND spacecraft to identify a sample of 152 well observed interplanetary coronal mass ejections and their MC counterparts. We compute various metrics using these data to address our questions.

Results. We find that the total specific energy (H) inside MCs is approximately equal to that in the background solar wind. We find that the the excess (thermal + magnetic) pressure and specific energy are not well correlated with the near-Earth propagation and expansion speeds. We find that the excess thermal+magnetic specific energy \geq the specific kinetic energy of the solar wind incident on 81–89 % of the MCs we study. This might explain how MCs retain their structural integrity and resist deformation by the solar wind bulk flow.

Key words. magnetohydrodynamics (MHD) – statistical – data analysis – coronal mass ejections (CMEs) – solar wind

1. Introduction

Earth-directed Coronal mass ejections (CMEs) originating from the solar corona are the primary drivers of geomagnetic storms. Realistic estimates of Sun-Earth CME propagation times and arrival velocities are therefore an important component of space weather forecasting. Understanding the dynamics of CMEs and the forces leading to their propagation and expansion is crucial to this endeavor. Approaches to this problem range from early analytical models for the entire Sun-Earth propagation (Chen 1996; Kumar and Rust 1996), semi-analytical models that apply only to the aerodynamic drag-dominated phase of the propagation (Cargill 2004; Sachdeva et al. 2015; Vršnak et al. 2013) to detailed 3D MHD models (Linker et al. 1999; Odstrcil and Pizzo 2009; Keppens et al. 2020; Tóth et al. 2012). Some efforts have focussed on characterizing the internal magnetic structure of the interplanetary counterparts of CMEs (ICMEs) (Klein and Burlaga 1982; Nieves-Chinchilla et al. 2016) and others have focussed on comprehensive characterizations of ICME properties (Richardson and Cane 2010; Temmer 2021; Forsyth et al. 2006).

Despite these advances, there are still some fairly basic issues that remain to be addressed in this area. CME expansion provides a concrete window into some of these issues. It is well

known that CMEs translate as well as expand as they travel through the heliosphere - CMEs are observed to expand in typical coronagraph fields of view (St. Cyr et al. 2000) and beyond (Lugaz et al. 2010; Webb et al. 2009). CME expansion has also been confirmed using *in-situ* observations in the heliosphere (Bothmer & Schwenn 1998; Wang & Richardson 2004) and near the Earth (Dasso et al. 2007). The expansion is thought to occur because the interior of the CME is over-pressured with respect to its surroundings (e.g., von Steiger and Richardson 2006; Scolini et al. 2019; Démoulin and Dasso 2009; Verbeke et al. 2022), although some contend that the expansion is an outcome of CME magnetic field rearrangement (Kumar and Rust 1996). Some authors (e.g., Gopalswamy et al. 2014, 2015; Kassa Dagneu et al. 2022), ask if the abundance of halo CMEs during solar cycle 24 is because the ambient solar wind pressure is generally lower, leading CMEs to be more over-pressured (with respect to the surroundings) than usual. CME expansion speeds are also known to be lower than the Alfvén speeds in the ambient solar wind (Klein and Burlaga 1982; Lugaz et al. 2020) - this is another instance of comparison between the CME plasma and that of the surrounding solar wind. CME identification using *in-situ* data also relies on a comparison between the CME and the ambient solar wind plasma - one of the well accepted criteria for

identifying near-Earth magnetic clouds is that it is a low plasma beta structure, relative to the background solar wind (Klein and Burlaga 1982; Lepping et al. 2003). Evidently, a comparison of the thermal and magnetic pressure inside CMEs (relative to the background solar wind) is an issue of considerable interest. In this paper, we use near-Earth *in-situ* data to compare the plasma inside a large sample of well-observed magnetic clouds (MCs) with respect to their surroundings. Besides comparing the thermal and magnetic pressures, we also compute the specific energy which is a conserved quantity in an ideal magnetized flow, and serves as a useful reference quantity. Such an exercise has not been carried out for a large sample of well-observed events to the best of our knowledge, and it allows us to reach a number of useful conclusions.

The data used in this study are described in § 2 and the total specific energy for an ideal magnetized fluid is discussed in § 3. The total specific energy inside the MC is compared with that in the ambient solar wind in § 4.1, while the thermal+magnetic specific energy inside MCs is compared with that in the ambient solar wind in § 4.2. We compare the thermal+magnetic pressure inside MCs with that in the ambient solar wind in § 4.3. The role of the excess thermal+magnetic specific energy and pressure in influencing MC propagation and expansion is discussed in § 4.4. We speculate how the excess thermal+magnetic specific energy could contribute to maintaining the structural integrity of MCs in § 5 and present the conclusions in § 6.

2. Data

We use *in-situ* data from the WIND spacecraft (<https://wind.nasa.gov/>) for this study. The WIND ICME catalogue (<https://wind.nasa.gov/ICMEindex.php>) provides a sample of well observed Earth directed ICMEs as observed by the WIND spacecraft (Nieves-Chinchilla *et al.* 2019; Nieves-Chinchilla *et al.* 2018) at 1 AU. In this paper, we limit our study to the analysis of magnetic clouds (MCs), which are the magnetically well-structured parts of ICMEs, with typically better defined boundaries and expansion speeds (Klein and Burlaga 1982). The MCs associated with these ICMEs are classified into different categories depending upon how well the observed plasma parameters fit the expectations of a static flux rope configuration. Of the ICMEs observed between 1995 and 2015 listed on the WIND website, we first shortlist MCs that are categorized as F+ and Fr events. These events best fit the expectations of the flux rope model (Nieves-Chinchilla *et al.* 2016, 2018). Fr events indicate MCs with a single magnetic field rotation between 90° and 180° and F+ events indicate MCs with a single magnetic field rotation greater than 180°. We further shortlist events that are neither preceded nor followed by any other ICMEs or ejecta within a window of two days ahead of and after the event under consideration. This helps us exclude possibly interacting events. Our final shortlist comprises 152 ICMEs, which are listed in Table A of the appendix. Since we intend to compare the pressure and specific energy inside MCs with that in the ambient/background solar wind, we need concrete criteria to define the background. Ideally, the background should be quiet and should be in the vicinity of the MC. Accordingly, we use two different solar wind backgrounds for each event. The first kind of background, which we call BG1, is a 24-hour window within 5 days preceding the event that satisfies the following conditions: a) the rms fluctuations of the solar wind velocity for this 24-hour period should not exceed 10% of the mean value b) the rms fluctuations of the total magnetic field for this 24-hour period should not exceed 20% of the mean value c) there are no magnetic field

rotations. We find that the average plasma beta in the background is at least 1.5 times higher than that in the MC. Criteria a) and b) ensure that the background is quiet. Criterion c) distinguishes between the background and the MC, since MCs are characterized by large rotations of magnetic field components and low plasma beta. The second background, which we call BG2, is a 24-hour period immediately preceding the event. We use the term ‘solar wind’ only for the ambient/background solar wind throughout this study.

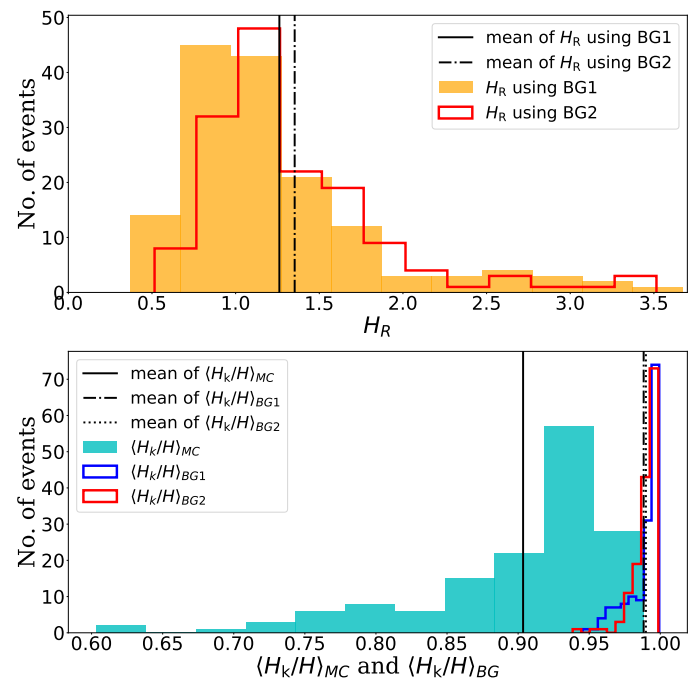


Fig. 1. Histograms of H_R and $\langle H_k/H \rangle$ for all the events listed in Table A. The top panel shows the histograms for H_R (Equation 8) with $\gamma = 5/3$ using two different backgrounds, BG1 and BG2. The mean, median and most probable value of H_R using BG1 are 1.26, 1.1 and 0.97 respectively. Using BG2, they are 1.36, 1.19 and 1.12 respectively. The histograms in the bottom panel display the ratio of H_k to H inside the MC ($\langle H_k/H \rangle_{MC}$) and in the backgrounds ($\langle H_k/H \rangle_{BG1}$, $\langle H_k/H \rangle_{BG2}$) using $\gamma = 5/3$. The mean, median and the most probable value of $\langle H_k/H \rangle_{MC}$ are 0.90, 0.92 and 0.94 respectively. The mean, median and the most probable value of $\langle H_k/H \rangle_{BG1}$ are 0.98, 0.99 and 0.995 respectively and those of $\langle H_k/H \rangle_{BG2}$ are 0.99, 0.99 and 0.996 respectively. The mean value of each histogram is marked by a vertical line.

3. The specific energy for an ideal magnetized fluid

In the lab frame, the conservative form of the ideal MHD energy equation is [(Equation 65.10, Chapter 8, Landau & Lifshitz 1987); (Chapter 4 of Boyd & Sanderson 2003; Kulsrud 2005)]

$$\frac{\partial E}{\partial t} = -\nabla \cdot \left[\frac{\rho v^2}{2} \mathbf{v} + \frac{\gamma}{\gamma - 1} P_{th} \mathbf{v} - \frac{(\mathbf{v} \times \mathbf{B}) \times \mathbf{B}}{4\pi} \right], \quad (1)$$

where E is the energy density (erg cm^{-3}) of a parcel of fluid, \mathbf{v} is the fluid velocity (cm s^{-1}), ρ is the mass density of the fluid (g cm^{-3}), P_{th} is the thermal pressure (including contributions from protons and electrons), γ is the polytropic index and \mathbf{B} is the total magnetic field. The term inside the square brackets on the right hand side (RHS) of Equation 1 represents the total energy flux ($\text{erg cm}^{-2} \text{s}^{-1}$). In what follows, we will write the energy flux as $\rho v H \hat{\mathbf{p}}$, where H is the total specific energy

(erg g⁻¹) and $\hat{\mathbf{p}}$ is the unit vector directed along the total energy flux. H contains contributions from the bulk motion of the fluid, the thermal energy and the magnetic field. The quantity

$$H_k \equiv (1/2)v^2 \quad (2)$$

is the specific kinetic energy (erg g⁻¹) of the fluid due to its bulk motion and

$$H_{th} \equiv \frac{\gamma}{\gamma - 1} \frac{P_{th}}{\rho} \quad (3)$$

is the specific thermal energy (erg g⁻¹) associated with the fluid. In order to understand the contribution to the specific energy from the magnetic field, we examine the Poynting flux (\mathbf{S}), which is the energy flux (erg cm⁻² s⁻¹) carried by the electromagnetic field, and is defined by

$$\begin{aligned} \mathbf{S} &\equiv (c/4\pi)\mathbf{E} \times \mathbf{B} = (1/4\pi)\mathbf{B} \times (\mathbf{v} \times \mathbf{B}) = (1/4\pi)[\mathbf{v}\mathbf{B}^2 - \mathbf{B}(\mathbf{v} \cdot \mathbf{B})] \\ &= (1/4\pi)\mathbf{v}_\perp B^2 = (1/4\pi)v_\perp B^2 \hat{\mathbf{n}}, \end{aligned} \quad (4)$$

where \mathbf{v}_\perp and \mathbf{v}_\parallel are the components of the fluid velocity perpendicular to and parallel to the magnetic field respectively and $\hat{\mathbf{n}}$ is the unit vector perpendicular to \mathbf{B} . Equation 4 assumes an infinitely conducting fluid and induction-only electric field. It follows from Equation 4 that the energy density (erg cm⁻³) associated with the magnetic field is $B^2/4\pi$ (Parker 2009). Accordingly, we define the specific energy (erg g⁻¹) associated with the magnetic field as

$$H_{mag} \equiv (B^2/4\pi\rho) \quad (5)$$

The quantity in the square brackets in Eq 1 is then

$$\begin{aligned} \rho(H_k + H_{th})(v_\parallel \hat{\mathbf{b}} + v_\perp \hat{\mathbf{n}}) + \rho H_{mag} v_\perp \hat{\mathbf{n}} &= \rho v_\perp (H_k + H_{th} + H_{mag}) \hat{\mathbf{n}} \\ + \rho v_\parallel (H_k + H_{th}) \hat{\mathbf{b}} &= \rho v \hat{\mathbf{p}} [\cos^2 \theta (H_k + H_{th})^2 + \\ \sin^2 \theta (H_k + H_{th} + H_{mag})^2]^{1/2} &= \rho v \hat{\mathbf{p}} H, \end{aligned}$$

where $\sin\theta \equiv v_\perp/v$, $\cos\theta \equiv v_\parallel/v$, $\hat{\mathbf{b}}$ is the unit vector along \mathbf{B} and $\hat{\mathbf{p}}$ is a unit vector in the direction (which is neither along the fluid streamlines nor along the magnetic field) along which the total energy flux is directed and

$$H \equiv [\cos^2 \theta (H_k + H_{th})^2 + \sin^2 \theta (H_k + H_{th} + H_{mag})^2]^{1/2}. \quad (6)$$

The angle α that $\hat{\mathbf{p}}$ makes with $\hat{\mathbf{b}}$ is given by

$$\tan \alpha = \frac{v_\perp (H_k + H_{th} + H_{mag})}{v_\parallel (H_k + H_{th})} \quad (7)$$

In steady state, the total energy is conserved in ideal MHD, which means the left hand side of Eq 1 is zero. Using Eq 6, this means that $\nabla \cdot (\rho v \hat{\mathbf{p}} H) = H \nabla \cdot (\rho v \hat{\mathbf{p}}) + (\rho v \hat{\mathbf{p}}) \cdot \nabla H = 0$. In steady state, mass conservation implies that $\nabla \cdot (\rho v \hat{\mathbf{p}}) = 0$, which means that $\rho v \hat{\mathbf{p}} \cdot \nabla H = 0$. In turn, this means that $\nabla H \perp \hat{\mathbf{p}}$ and H (Eq 6) is constant along $\hat{\mathbf{p}}$. This is unlike an unmagnetized fluid, where the total specific energy (often referred to as the Bernoulli parameter) is equal to the sum of H_k and H_{th} and is conserved along the velocity streamlines. The direction $\hat{\mathbf{p}}$ along which H is conserved (in ideal MHD) need not coincide with the line of the spacecraft intercept. Therefore, we only compare the average value of H inside MCs with its average value in the background solar wind (rather than regarding H as a conserved quantity along the spacecraft line of intercept). This is in the

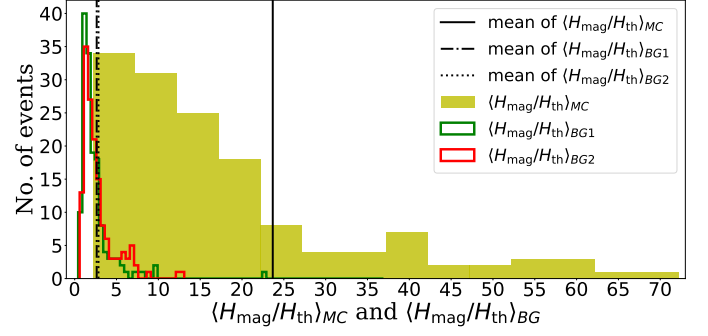


Fig. 2. Histograms of $\langle H_{mag}/H_{th} \rangle$ (with $\gamma = 5/3$) inside the MC and in the two backgrounds, BG1 and BG2, for all the events listed in Table A. The mean, median and the most probable value of $\langle H_{mag}/H_{th} \rangle_{MC}$ are 23.68, 14.13 and 4.78 respectively. The mean, median and most probable value of $\langle H_{mag}/H_{th} \rangle_{BG1}$ are 2.63, 1.73 and 1.10 respectively while for $\langle H_{mag}/H_{th} \rangle_{BG2}$ they are 2.84, 2.12 and 1.63 respectively. The mean value of each histogram is marked by a vertical line.

same spirit in which the thermal and magnetic pressures inside CMEs are compared with those in the background solar wind. Furthermore, H does not include non-ideal effects such as losses due to viscous and resistive heating. However, the bulk solar wind is characterized by very high fluid and magnetic Reynolds numbers, which is why ideal MHD is usually considered to be an adequate description for characterizing the solar wind. Even the plasma inside magnetic clouds has very high Lundquist numbers (Bhattacharjee et al. 2022), justifying an ideal MHD treatment. Finally, the expression for H (Eq 6) uses a polytropic index γ . The appropriate value to use for γ inside ICMEs or MCs is not clear. A value of 5/3 would imply that the ICME plasma is cooling adiabatically and needs to be heated to maintain its temperature (Kumar and Rust 1996), whereas a value of 1.2 implies efficient thermal conduction to the interior of the ICME from the solar corona and little additional heating (Chen 1996). A recent study using Helios and Parker Solar Probe (PSP) data postulates a polytropic index ranging from 1.35 to 1.57 for solar wind protons and an index ranging from 1.21 to 1.29 for solar wind electrons (Dakeyo et al. 2022). Another study using PSP data (Nicolaou et al. 2020) claims a polytropic index $\approx 5/3$ for the solar wind plasma. The polytropic index of the CME plasma is thought to range from 1.35 to 1.8 (Mishra and Wang 2018). In view of this, we use two values for γ (5/3 and 1.2) in our calculations.

4. Comparing H inside MCs and the background solar wind

The *in-situ* data from WIND spacecraft (<https://wind.nasa.gov/>) provides a detailed time profile of all the components of the plasma velocity (\mathbf{v}), proton number density (n) and all components of the magnetic field (\mathbf{B}) in the spacecraft reference frame. We will use the terms “plasma” and “magnetized fluid” interchangeably in the rest of the paper; therefore the term “plasma velocity” can be taken to mean the quantity \mathbf{v} introduced in § 3. The data allow us to also compute the angle (θ) between the plasma velocity \mathbf{v} and the magnetic field \mathbf{B} . The data also provide the time profile of the plasma thermal pressure (P_{th}) which includes contributions from protons and electrons (https://omniweb.gsfc.nasa.gov/ftpbrowser/bow_derivation.html). Assuming the electron

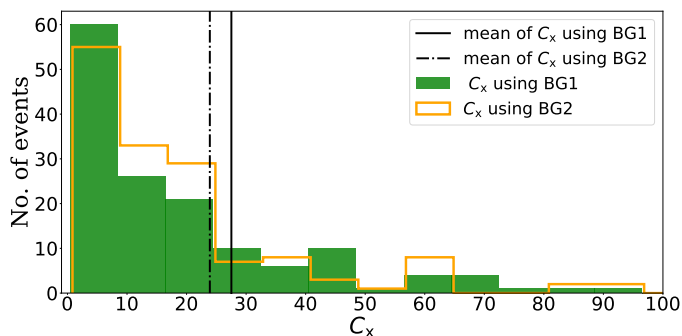


Fig. 3. Histograms of C_x (Equation 9) with $\gamma = 5/3$ and using the two backgrounds, BG1 and BG2. The mean, median and the most probable value of C_x using BG1 are 27.53, 11.09 and 2.48 respectively while for BG2, they are 23.91, 14.02 and 4.36 respectively. The mean value for each histogram is marked by a vertical line. The maximum value shown on the x axis is limited to 100 for zooming in on the histogram peaks.

number density to be equal to the proton number density (so that $\rho = n(m_p + m_e)$ where m_p and m_e are the proton and electron masses respectively) and adopting two values for the polytropic index ($\gamma = 5/3$ and 1.2), the data allow us to calculate H (Eq 6) along the line of spacecraft intercept.

4.1. $\langle H \rangle_{MC}$ vs $\langle H \rangle_{BG}$

We compare the average value of H inside MCs with that in the background solar wind using the quantity

$$H_R \equiv \frac{\langle H \rangle_{MC}}{\langle H \rangle_{BG}} \quad (8)$$

where $\langle \rangle_{MC}$ and $\langle \rangle_{BG}$ represent averages inside the MC and the

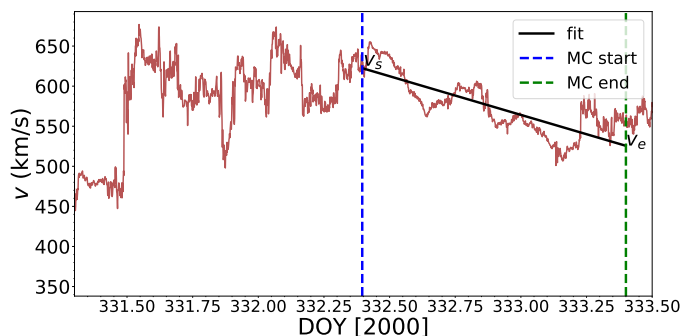


Fig. 4. Velocity (v) profile as a function of time for event 54 in our dataset (Table A). The start time (t_s) and end time (t_e) of the MC are marked by blue and green dashed lines respectively. The black solid line shows a linear fit to v . v_s and v_e denote the value of the fit at t_s and t_e respectively. We compute the MC expansion speed v_{exp} (Equation 11) using v_s and v_e .

background respectively. We compute H_R using two different backgrounds (BG1 and BG2) which are described in § 2. We first describe the results obtained using $\gamma = 5/3$. The histograms of H_R for all the events in our sample is shown in the top panel of Figure 1. The mean, median and the most probable value of H_R using BG1 are 1.26, 1.1 and 0.97 respectively. Using BG2 they are 1.36, 1.19 and 1.12 respectively. The bottom panel of Figure 1 shows a histogram of the ratio $\langle H_k/H \rangle$ inside the MC and in the two backgrounds, BG1 and BG2. The mean, median and most probable value of $\langle H_k/H \rangle_{MC}$ are 0.90, 0.92 and 0.94

respectively. The mean, median and the most probable values of $\langle H_k/H \rangle_{BG}$ are not very different; they are 0.98, 0.99 and 0.995 respectively for BG1 and 0.99, 0.99 and 0.996 for BG2. We note that though BG1 and BG2 are selected based on different criteria, the results are quite similar. Using $\gamma = 1.2$, the mean, median and most probable values of H_R are 1.27, 1.09 and 0.93 respectively (using BG1) and 1.36, 1.19 and 1.14 respectively (using BG2). Using $\gamma = 1.2$ we find that the mean, median and most probable value of $\langle H_k/H \rangle_{MC}$ are 0.89, 0.91 and 0.92 respectively. The mean, median and most probable value of $\langle H_k/H \rangle_{BG}$ for both the backgrounds are 0.98, 0.99 and 0.992 respectively. The main conclusions at this point are i) the total specific energy (H) inside the MC is approximately the same as that in the background, ii) $H_k \approx H$, both inside the MC and in the background. iii) the choice of the background and polytropic index does not affect these broad conclusions.

4.2. Comparing the thermal+magnetic specific energy inside MCs and the background

Having shown that the contribution from the kinetic energy term (H_k) dominates the specific energy both in the background solar wind and inside the MC, we now compare the thermal+magnetic contributions to the specific energy in the MC and the background using the metric

$$C_x \equiv \frac{\langle \epsilon \rangle_{MC}}{\langle \epsilon \rangle_{BG}}, \quad \text{where } \epsilon \equiv [H_{th}^2 \cos^2 \theta + (H_{th} + H_{mag})^2 \sin^2 \theta]^{1/2} \quad (9)$$

The values of C_x are listed in Table B.4. As mentioned earlier, $\langle \rangle_{MC}$ and $\langle \rangle_{BG}$ represent averages inside the MC and the background solar wind respectively. The quantity ϵ is the thermal + magnetic contribution to the specific energy (often called the enthalpy). The thermal contribution to the specific energy in an unmagnetized fluid is well known to be $\gamma P_{th}/(\gamma - 1)$, and the expression for ϵ (used in Eq 9) is written following the reasoning in Eq 6. The histograms of C_x in Figure 3 have a mean, median and most probable value of 27.53, 11.09 and 2.48 respectively (using BG1) and 23.91, 14.02 and 4.36 respectively (using BG2). The mean values (which are relatively high in comparison to the median and most probable value) are biased by $\approx 40\%$ of events for both the backgrounds. Our results show that the thermal + magnetic specific energy inside the MC is generally higher than that of the background. If we use $\gamma = 1.2$ instead of 5/3, we find the mean, median and the most probable values of C_x are 18.48, 8.30 and 4.70 respectively (using BG1) and 16.51, 9.89 and 3.32 respectively (using BG2). The statistical picture of C_x thus do not differ significantly on using $\gamma = 1.2$. With $\gamma = 5/3$, the mean, median and the most probable value of $\langle H_{mag}/H_{th} \rangle$ inside MCs are 23.68, 14.13 and 4.78 respectively, while it is only 2.63, 1.73 and 1.10 respectively inside BG1 and 2.84, 2.12 and 1.63 inside BG2 (Figure 2). With $\gamma = 1.2$, $\langle H_{mag}/H_{th} \rangle$ is smaller (in comparison to the values with $\gamma = 5/3$) both inside the MC and in the backgrounds. The mean, median and the most probable value of $\langle H_{mag}/H_{th} \rangle_{MC}$ are 9.87, 5.89 and 2.43 respectively, and it is 1.10, 0.72 and 0.46 respectively (for BG1) and 1.19, 0.88 and 0.59 respectively (for BG2). The enhancement of C_x inside MCs is thus primarily due to the magnetic fields.

4.3. Comparing the thermal+magnetic pressure inside MCs and the background

There are several studies concerning the difference between the thermal+magnetic pressure $P_{th} + P_{mag}$ inside CMEs and the ambient solar wind (Burlaga *et al.* 1981; Moldwin *et al.* 2000;

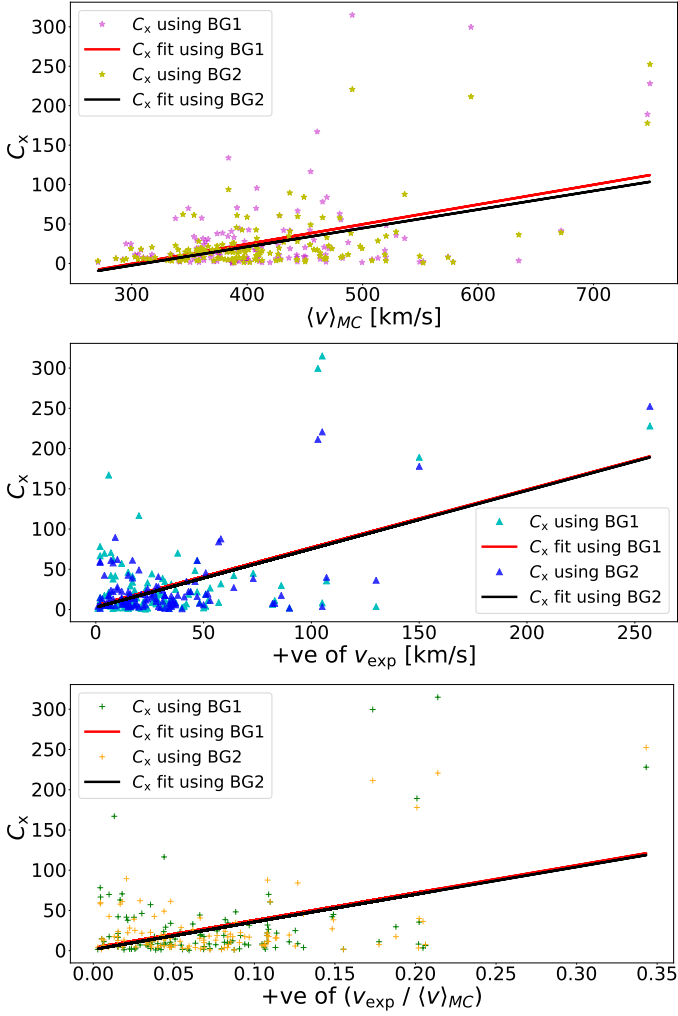


Fig. 5. Scatterplots of C_x with MC propagation and expansion speeds for all the events listed in Table A. The top panel is the scatterplot between C_x (estimated using $\gamma = 5/3$) (Equation 9) and the MC propagation speed ($\langle v \rangle_{MC}$). The correlation coefficient between C_x and $\langle v \rangle_{MC}$ are $r = 0.43$ with $p = 3.5 \times 10^{-8}$ (for BG1) and $r = 0.51$ with $p = 1.8 \times 10^{-11}$ (for BG2). The equation of the fitted lines corresponding to BG1 and BG2 are $y = 0.25x - 75.65$ and $y = 0.24x - 73.28$ respectively. The middle panel is the scatterplot between C_x (computed using $\gamma = 5/3$) and the MC expansion speed (v_{exp}), only for events with $v_{exp} > 0$. The correlation coefficients are $r = 0.50$ with $p = 5.73 \times 10^{-9}$ for BG1 and $r = 0.63$ with $p = 1.9 \times 10^{-14}$ for BG2. The equation of fitted lines are $y = 0.72x + 4.82$ and $y = 0.73x + 2.73$ corresponding to BG1 and BG2 respectively. The bottom panel is the scatterplot between C_x (calculated using $\gamma = 5/3$) and $v_{exp}/\langle v \rangle_{MC}$ (only for events with $v_{exp} > 0$). The correlation coefficients are $r = 0.40$ with $p = 7.8 \times 10^{-6}$ (for BG1) and $r = 0.50$ with $p = 1.2 \times 10^{-8}$ (for BG2). The equation of the fitted lines are $y = 342.6x + 3.36$ (for BG1) and $y = 341.71x + 1.46$ (for BG2). The small p-values imply a high statistical confidence in computing the r values in all the three cases.

Jian *et al.* 2005; Démoulin and Dasso 2009; Gopalswamy *et al.* 2015). It is often speculated that the reason ICMEs expand internally is because they are overpressured with respect to the ambient solar wind (Scolini *et al.* 2019). Gopalswamy *et al.* (2015) and Mishra, Doshi, and Srivastava (2021) examined if ICMEs were more overpressured during relatively weaker solar cycles, leading to more halo CMEs during such cycles. We therefore compute the following coefficient for the events in our sample

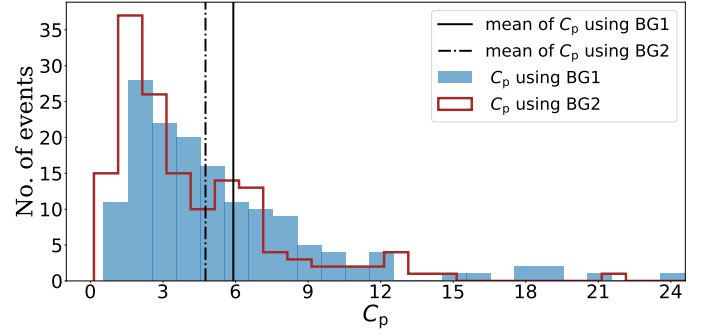


Fig. 6. Histograms of C_p (Equation 10) using two different backgrounds, BG1 and BG2. The mean, median and the most probable value of C_p with BG1 are 5.90, 4.29 and 2.39 respectively and the mean, median and the most probable value of C_p with BG2 are 4.76, 3.02 and 1.64 respectively. The mean value for each histogram is marked by a vertical line. The maximum value shown on the x axis is limited to 24.5 in order to zoom in on the histogram peaks.

using BG1 and BG2:

$$C_p \equiv \frac{\langle P_{mag} + P_{th} \rangle_{MC}}{\langle P_{mag} + P_{th} \rangle_{BG}} \quad (10)$$

where P_{mag} ($= \mathbf{B}^2/8\pi$) is the magnetic pressure and P_{th} is the thermal pressure of the plasma. The thermal pressure P_{th} includes contributions from both protons and electrons and $\langle \rangle_{MC}$ and $\langle \rangle_{BG}$ have their usual meanings. The C_p values are listed in Table B.4 and histograms for C_p are shown in Figure 6. The mean, median and the most probable value for C_p using BG1 are 5.90, 4.29 and 2.39 respectively and using BG2, they are 4.76, 3.02 and 1.64 respectively. By comparison, Gopalswamy *et al.* (2015) find that the total pressure ratio between the MCs and the ambient solar wind is ≈ 3 for their set of near-Earth CMEs. The results thus suggest that the average magnetic+thermal pressure inside near-Earth MCs is appreciably higher than that of the solar wind background. The polytropic index γ has no bearing on C_p .

4.4. Is the excess thermal+magnetic specific energy and pressure inside MCs correlated with near-Earth expansion and propagation speeds?

Just as several studies ask if the excess pressure inside ICMEs leads to their expansion (see e.g., von Steiger and Richardson 2006; Scolini *et al.* 2019; Démoulin and Dasso 2009; Verbeke *et al.* 2022), it is natural to ask if the enhanced thermal+magnetic specific energy inside MCs result in their expansion. We compute the MC expansion speed (Nieves-Chinchilla *et al.* 2018)

$$v_{exp} = \frac{1}{2}(v_s - v_e) \quad (11)$$

for each MC in our sample. The quantities v_s and v_e are the speeds at the start and at the end of the MC respectively. Figure 4 shows an example of a linear fit that is used to compute v_s , v_e and consequently v_{exp} . We note that v_{exp} for $\approx 20\%$ of MCs in our sample is negative; i.e., they contract, rather than expand. Figure 5 shows scatterplots between C_x (estimated using both BG1 and BG2) and the near-Earth MC propagation speed $\langle v \rangle_{MC}$ (panel a) and v_{exp} (panel b) for expanding MCs (i.e.; those for which $v_{exp} > 0$). The linear correlation coefficient (r) between C_x and the MC propagation speed ($\langle v \rangle_{MC}$) is 0.43 with a p-value of 3.5×10^{-8} with BG1 and $r = 0.51$ with $p = 1.8 \times 10^{-11}$ with

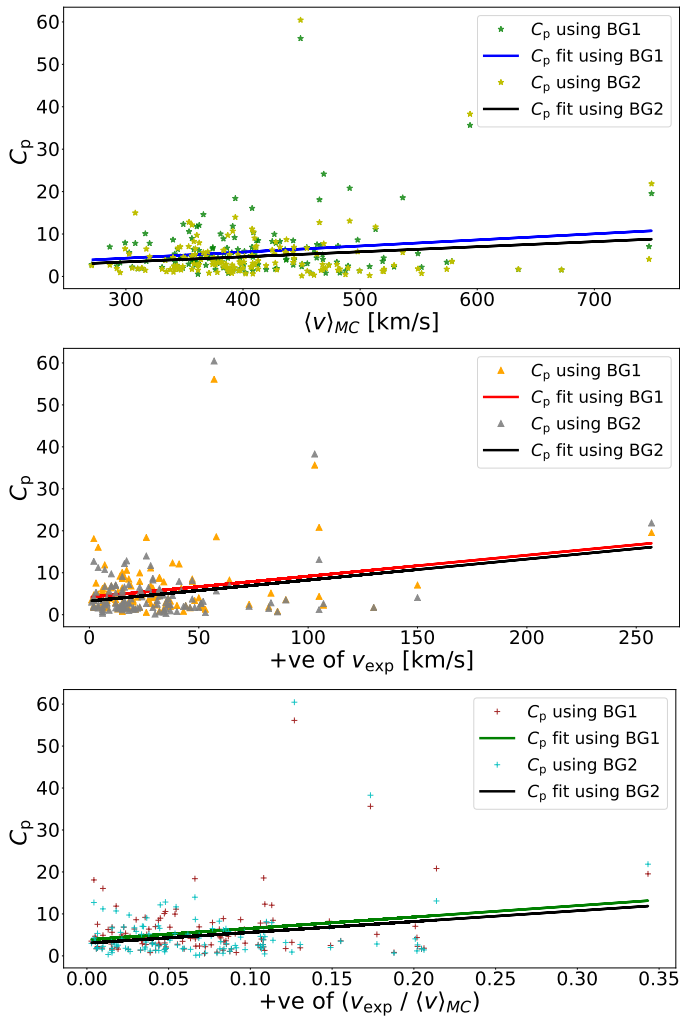


Fig. 7. Scatterplots of C_p with MC propagation and expansion speeds for all the events listed in Table A. The top panel is the scatterplot between C_p (Equation 10) and the MC propagation speed ($\langle v \rangle_{MC}$). The correlation coefficient between C_p and $\langle v \rangle_{MC}$ is $r = 0.18$ with $p = 2 \times 10^{-2}$ (for BG1) and $r = 0.15$ with $p = 5 \times 10^{-2}$ (for BG2). The equation of the fitted lines corresponding to BG1 and BG2 are $y = 0.01x - 0.004$ and $y = 0.01x - 0.1$ respectively. The middle panel is the scatterplot between C_p and the MC expansion speed (v_{exp}), only for events with $v_{exp} > 0$. The correlation coefficients are $r = 0.25$ with $p = 2 \times 10^{-3}$ for BG1 and $r = 0.25$ with $p = 5 \times 10^{-3}$ for BG2. The equation of the fitted lines are $y = 0.05x + 4.5$ and $y = 0.05x + 3.26$ for BG1 and BG2 respectively. The bottom panel is the scatterplot between C_p and $v_{exp}/\langle v \rangle_{MC}$, only for events with $v_{exp} > 0$. The correlation coefficients are $r = 0.23$ with $p = 6 \times 10^{-3}$ (for BG1) and $r = 0.22$ with $p = 10^{-3}$ (for BG2). The equation of the fitted lines are $y = 25.3x + 4.30$ (for BG1) and $y = 25.78x + 3.02$ (for BG2). The small p-values indicate a sufficiently high statistical confidence in estimating the r values for all the three cases.

BG2. The linear correlation coefficient (r) between C_x and v_{exp} for the expanding events is 0.50 and the corresponding p-value is 5.73×10^{-9} (using BG1) and $r = 0.63$ with $p = 1.9 \times 10^{-14}$ (using BG2). The correlation coefficient between C_x and $v_{exp}/\langle v \rangle$ (considering only events with positive v_{exp}) $r = 0.40$ with a p-value 7.8×10^{-6} for BG1 and $r = 0.50$ with $p = 1.2 \times 10^{-8}$ for BG2. Our findings suggest that C_x is only moderately correlated with the near-Earth MC propagation and expansion speed. The low values for p in all the cases indicate a high statistical significance for these results.

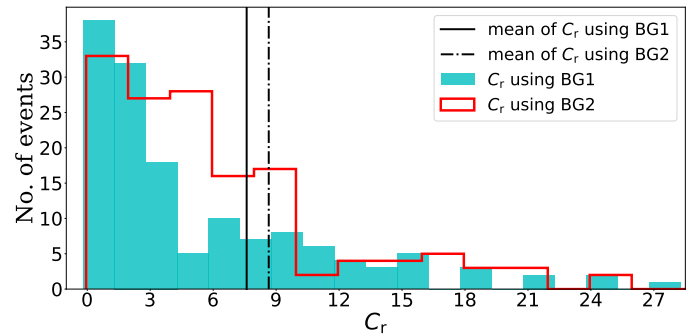


Fig. 8. Histograms of C_r (Equation 12) with $\gamma = 5/3$ using both the backgrounds (BG1 and BG2). The mean, median and the most probable value of C_r are 7.61, 3.33 and 1.16 respectively for BG1 and 8.65, 4.65 and 2.25 respectively for BG2. The mean value of each histogram is marked by a vertical line. The maximum value shown on the x axis is limited to 28 for zooming in on the histogram peaks.

We next study if/how the overpressure parameter C_p is correlated with the near-Earth MC expansion and propagation speeds. Panel (a) of Figure 7 shows the scatterplot between C_p (using both BG1 and BG2) and the MC propagation speed. The correlation is low ($r = 0.18$, p -value = 2×10^{-2} using BG1 and $r = 0.15$, $p = 5 \times 10^{-2}$ using BG2). The correlation between C_p and the MC expansion speed of the expanding MCs ($v_{exp} > 0$) is also low (panel b of Figure 7, $r = 0.25$, p -value = 2×10^{-3} using BG1 and $r = 0.25$ with $p = 5 \times 10^{-3}$). Finally, we note that the correlation coefficient between C_p and $v_{exp}/\langle v \rangle_{MC}$ for the expanding MCs (panel c of Figure 7) are $r = 0.23$ and the p -value is 6×10^{-3} for BG1 and $r = 0.22$ with $p = 10^{-3}$ for BG2. Evidently, C_p is rather poorly correlated with MC expansion and propagation speeds. This might be because we are using speeds measured at the position of the WIND observation, whereas most of the CME expansion probably occurs closer to the Sun (Verbeke et al. 2022).

5. Does the excess thermal+magnetic specific energy in MCs make them appear “rigid”?

The main results we have obtained until now are that i) the total specific energy inside the MC \approx that in the background, and ii) the sum of the thermal and magnetic (specific) energies is higher inside the MC as compared to the background. By way of trying to understand point ii) better, we define the following coefficient:

$$C_r = \frac{\langle \epsilon \rangle_{MC} - \langle \epsilon \rangle_{BG}}{\langle (1/2)u^2 \rangle_{BG}}, \quad (12)$$

where ϵ is defined in Eq 9, $\mathbf{u} \equiv \mathbf{v} - \langle \mathbf{v} \rangle_{MC}$ is the solar wind velocity in the frame of the MC and the other notations carry their usual meanings. The quantity $\langle (1/2)u^2 \rangle_{BG}$ denotes the specific kinetic energy of the oncoming solar wind incident on the MC as discerned by an observer moving with the average MC speed. The quantity C_r (Equation 12) thus compares the excess thermal+magnetic specific energy in the MC (relative to the background) with the specific kinetic energy of the solar wind impinging on it. If $C_r \gtrsim 1$, it means that the excess thermal + magnetic specific energy in the MC is greater than the specific kinetic energy of the oncoming solar wind - suggesting that the MC can resist deformation by the solar wind, somewhat like a rigid body. A way to understand C_r is as follows: imagine an inflated balloon placed in a stream of cold air. There are no magnetic fields, and

so $H_{\text{mag}} = 0$. Since the air stream is cold, $\langle H_{\text{th}} \rangle_{\text{BG}}$ is zero and the only term in the numerator of Eq 12 is $\langle H_{\text{th}} \rangle_{\text{MC}}$. The metric C_{r} thus compares the thermal specific energy due of the gas inside the balloon with the specific kinetic energy of the cold air stream incident on it. If $C_{\text{r}} \geq 1$, the balloon can resist deformation due to the incident air stream relatively better (i.e., it behaves more like a well-inflated soccer ball) and vice-versa.

The C_{r} values for all the events in our dataset are listed in Table B.4. The histogram of C_{r} for all the events using $\gamma = 5/3$ and both the backgrounds (BG1 and BG2) is shown in Figure 8. With BG1, we find that the mean, median and most probable values of C_{r} histogram are 7.61, 3.33 and 1.16 respectively, and 81% of the events have $C_{\text{r}} \geq 1$. Using BG2, the mean, median and most probable values are 8.65, 4.66 and 2.25 respectively and 89.5% of the events have $C_{\text{r}} \geq 1$. If we assume $\gamma = 1.2$ (instead of $5/3$), the mean, median and most probable values of C_{r} are 8.09, 3.55 and 1.12 respectively with BG1, and 9.50, 5.29 and 2.29 respectively with BG2. The choice of γ does not affect our results substantially.

Furthermore, the magnetic energy is typically higher than the thermal energy inside MCs, (Figure 2) suggesting that CME magnetic fields are primarily responsible for $C_{\text{r}} \geq 1$. Our findings are in keeping with those of Lynnyk et al. (2011) who state “If the magnetic field inside the ICME/MC is much stronger than that in the ambient solar wind, the ICME/MC cross-section is closer to circular.” MCs with more circular cross sections are probably ones which are relatively more rigid; i.e., ones which probably have $C_{\text{r}} \geq 1$, and have resisted deformation by the solar wind to more elongated shapes.

An issue related to the rigidity of MCs is the widely used CME aerodynamic drag law (Cargill 2004; Vršnak et al. 2009, 2013)

$$F_{\text{D}} = C_{\text{D}} A \rho |u| u \quad (13)$$

which is a hydrodynamic drag law applicable to high Reynolds number flows past *solid/rigid bodies* (Landau & Lifshitz 1987). In Equation 13, F_{D} is the drag force, u is the velocity of the background fluid as viewed by an observer comoving with the body, A is the cross-sectional area subtended by the body to the flow, ρ is the mass density of the background fluid and C_{D} is a dimensionless proportionality constant. By contrast, the high Reynolds number drag law for flows past deformable bubbles looks like $F_{\text{D}} \propto u$ (Landau & Lifshitz 1987; Moore 1959, 1963; Kang and Leal 1988). Although the $F_{\text{D}} \propto u$ resembles the Stokes law, which is applicable for laminar/low Reynolds number flows past solid bodies, it is in fact a high Reynolds number law for flows past deformable bubbles. Bubbles are distinct from solid bodies in that the total velocity does not vanish on their surface, as it does for solid bodies. We note that some studies of CME dynamics do adopt $F_{\text{D}} \propto u$ (Vršnak and Gopalswamy 2002; Maloney and Gallagher 2010). Although the form of the widely adopted CME aerodynamic drag law arises from an amalgamation of several MHD effects (Lin and Chen 2022), the simplest interpretation of Eq 13 is still that of a high Reynolds number, solid/rigid body law. Our finding $C_{\text{r}} \geq 1$ (for over 89 % of the MCs we study) might be a possible justification for the solid body premise, even for CMEs, which are obviously far from solid bodies in the usual sense of the word.

6. Conclusions and discussion

CME evolution through the heliosphere is thought to be strongly influenced by the difference in the (thermal + magnetic) pressures inside the CME and outside, in the ambient solar wind. In

this paper we compare the average value of the total specific energy H (Eq 6) inside MCs and the background solar wind using the near-Earth *in-situ* data from the WIND spacecraft for a set of 152 well observed MCs. The quantity H contains contributions from the kinetic energy due to the bulk flow (H_{k}), the thermal energy (H_{th}) and the magnetic energy (H_{mag}). We also compare the thermal+magnetic pressure inside MCs with the background solar wind. We use two different ambient solar wind backgrounds for our comparisons and also use two different values for the polytropic index γ . Our main conclusions are as follows:

1. The average value of H inside MCs, $\langle H \rangle_{\text{MC}} \approx$ the average value in the ambient solar wind ($\langle H \rangle_{\text{BG}}$) (§ 4.1, Figure 1). The bulk flow kinetic energy contribution $H_{\text{k}} \approx H$, both inside the MCs and in the ambient solar wind. This is the primary reason for $\langle H \rangle_{\text{MC}} \approx \langle H \rangle_{\text{BG}}$.
2. The average thermal+magnetic specific energy inside near-Earth MCs substantially exceeds that in the background solar wind (§ 4.2). Similarly, the average $P_{\text{th}} + P_{\text{mag}}$ inside near-Earth MCs is greater than that in the solar wind background (§ 4.3). These conclusions are broadly consistent with the findings of Gopalswamy *et al.* (2015) and Mishra, Doshi, and Srivastava (2021).
3. We find that the excess thermal+magnetic energy inside MCs is moderately correlated with MC near-Earth propagation and expansion speeds, while the correlation is rather poor for the excess thermal+magnetic pressure (§ 4.4). Summarizing, neither the excess enthalpy nor total pressure seems to be well correlated with the near-Earth MC propagation and expansion speeds. This might be because most of the expansion occurs closer to the Sun (Odstrčil & Pizzo 1999; Gopalswamy *et al.* 2014; Verbeke *et al.* 2022) and/or because magnetic field rearrangement is the primary reason for expansion (Kumar and Rust 1996).
4. We find that the excess thermal+magnetic specific energy inside MCs \geq the specific kinetic energy of the solar wind impinging on them for 81–89% of the events we study (§ 5). This suggests how MCs might be able to resist deformation by the solar wind, and might suggest a justification for the popular “rigid body” CME aerodynamic drag law (Equation 13).

Our results are based only on *in-situ* data at the position of the WIND measurements (i.e., at 1 AU). It would be interesting to carry out similar calculations using *in-situ* data closer to the Sun from the PSP (Weiss *et al.* 2020; Nieves-Chinchilla *et al.* 2022). This would yield insights on the evolution of CMEs through the heliosphere.

Acknowledgements. DB acknowledges the PhD studentship from Indian Institute of Science Education and Research, Pune. We acknowledge a detailed review by an anonymous referee that helped us improve the manuscript.

References

- Bhattacharjee D., Subramanian P., Bothmer V., Nieves-Chinchilla T., Vourlidas A., 2022, *SoPh*, 297, 45. doi:10.1007/s11207-022-01982-x
- Bothmer V., Schwenn R., 1998, *AnGeo*, 16, 1. doi:10.1007/s00585-997-0001-x
- Boyd T. J. M., Sanderson J. J., 2003, *phpl.book*, 544
- Burlaga, L., Sittler, E., Mariani, F., and Schwenn, R.: 1981, *Journal of Geophysical Research* **86**, 6673. doi:10.1029/JA086iA08p06673.
- Cargill, P. J., Chen, J., Spicer, D. S., et al. 1995, *Geophys. Res. Lett.*, 22, 647. doi:10.1029/95GL00013
- Cargill, P. J., & Schmidt, J. M. 2002, *Annales Geophysicae*, 20, 879
- Cargill, P. J. 2004, *Sol. Phys.*, 221, 135
- Chané E., Schmieder B., Dasso S., Verbeke C., Grison B., Démoulin P., Poedts S., 2021, *A&A*, 647, A149. doi:10.1051/0004-6361/202039867
- Chen J., Garren D. A., 1993, *GeoRL*, 20, 2319. doi:10.1029/93GL02426

- Chen, J.: 1996, *Journal of Geophysical Research* **101**, 27499. doi:10.1029/96JA02644.
- Chen, P.F.: 2011, *Living Reviews in Solar Physics* **8**, 1. doi:10.12942/lrsp-2011-1.
- Dakeyo, Maksimovic, Démoulin, Halekas, and Stevens: 2022, *arXiv e-prints*, arXiv:2207.03898.
- Démoulin, P. and Dasso, S.: 2009, *Astronomy and Astrophysics* **498**, 551. doi:10.1051/0004-6361/200810971.
- Davies E. E., Möstl C., Owens M. J., Weiss A. J., Amerstorfer T., Hinterreiter J., Bauer M., et al., 2021, A&A, 656, A2. doi:10.1051/0004-6361/202040113
- Dasso S., Nakwacki M. S., Démoulin P., Mandrini C. H., 2007, *SoPh*, 244, 115. doi:10.1007/s11207-007-9034-2
- Forsyth, R.J., Bothmer, V., Cid, C., Crooker, N.U., Horbury, T.S., Kecskemety, K., and, ...: 2006, *Space Science Reviews* **123**, 383. doi:10.1007/s11214-006-9022-0.
- Gopalswamy, N., Akiyama, S., Yashiro, S., Xie, H., Mäkelä, P., and Michalek, G.: 2014, *Geophys. Res. Lett.* **41**, 2673. doi:10.1002/2014GL059858.
- Gopalswamy, N., Yashiro, S., Xie, H., Akiyama, S., and Mäkelä, P.: 2015, *Journal of Geophysical Research (Space Physics)* **120**, 9221. doi:10.1002/2015JA021446.
- Groth, C.P.T., De Zeeuw, D.L., Gombosi, T.I., and Powell, K.G.: 2000, *Journal of Geophysical Research* **105**, 25053. doi:10.1029/2000JA900093.
- Guo, J., Feng, X., Emery, B.A., Zhang, J., Xiang, C., Shen, F., and, ...: 2011, *Journal of Geophysical Research (Space Physics)* **116**, A05106. doi:10.1029/2011JA016490.
- Hidalgo M. A., 2003, JGRA, 108, 1320. doi:10.1029/2002JA009818
- Jian, L., Russell, C.T., Gosling, J.T., and Luhmann, J.G.: 2005, *Solar Wind 11/SOHO 16, Connecting Sun and Heliosphere* **592**, 731.
- Jian L., Russell C. T., Luhmann J. G., Skoug R. M., 2008, *AdSpR*, 41, 259. doi:10.1016/j.asr.2007.03.023
- Kang, I.S. and Leal, L.G.: 1988, *Physics of Fluids* **31**, 233. doi:10.1063/1.866852.
- Kassa Dagneu, F., Gopalswamy, N., Belay Tessema, S., Akiyama, S., and Yashiro, S.: 2022, *arXiv e-prints*, arXiv:2208.03536.
- Keppens, R., Teunissen, J., Xia, C., and Porth, O.: 2020, *arXiv e-prints*, arXiv:2004.03275.
- Kilpua, E., Isavnin, A., Vourlidas, A., Koskinen, H., and Rodriguez, L.: 2013, *EGU General Assembly Conference Abstracts*.
- Klein, L.W. and Burlaga, L.F.: 1982, *Journal of Geophysical Research* **87**, 613. doi:10.1029/JA087iA02p00613.
- Klein K. G., Howes G. G., TenBarge J. M., Bale S. D., Chen C. H. K., Salem C. S., 2012, *ApJ*, 755, 159. doi:10.1088/0004-637X/755/2/159
- Kumar, A. and Rust, D.M.: 1996, *Journal of Geophysical Research* **101**, 15667. doi:10.1029/96JA00544.
- Kundu, P. K., & Cohen, I. M. 2008, *Fluid Mechanics: Fourth Edition*. Edited by Pijush K. Kundu and Ira M. Cohen with contributions by P. S. Ayyaswamy and H. H. Hu. ISBN 978-0-12-373735-9. Published by Academic Press
- Kulsrud R. M., 2005, *Plasma Physics for Astrophysics*
- Landau, L. D., & Lifshitz, E. M. 1987, *Fluid Mechanics*. Second Edition. 1987. Pergamon
- Lepping R. P., Berdichevsky D. B., Szabo A., Arqueros C., Lazarus A. J., 2003, *SoPh*, 212, 425. doi:10.1023/A:1022938903870
- Lin, C.-H. and Chen, J.: 2022, *Journal of Geophysical Research (Space Physics)* **127**, e28744. doi:10.1029/2020JA028744.
- Linker, J.A., Mikić, Z., Biesecker, D.A., Forsyth, R.J., Gibson, S.E., Lazarus, A.J., and, ...: 1999, *Journal of Geophysical Research* **104**, 9809. doi:10.1029/1998JA900159.
- Lionello, R., Downs, C., Linker, J. A., et al. 2013, *ApJ*, 777, 76. doi:10.1088/0004-637X/777/1/76
- Lugaz N., Hernandez-Charpak J. N., Roussev I. I., Davis C. J., Vourlidas A., Davies J. A., 2010, *ApJ*, 715, 493. doi:10.1088/0004-637X/715/1/493
- Lugaz, N. & Roussev, I. I. 2011, *Journal of Atmospheric and Solar-Terrestrial Physics*, 73, 1187. doi:10.1016/j.jastp.2010.08.016
- Lugaz N., Salman T. M., Winslow R. M., Al-Haddad N., Farrugia C. J., Zhuang B., Galvin A. B., 2020, *ApJ*, 899, 119. doi:10.3847/1538-4357/aba26b
- Lynnyk A., Šafránková J., Němeček Z., Richardson J. D., 2011, *P&SS*, 59, 840. doi:10.1016/j.pss.2011.03.016
- Maloney, S.A. and Gallagher, P.T.: 2010, *The Astrophysical Journal* **724**, L127. doi:10.1088/2041-8205/724/2/L127.
- Manchester W. B., Gombosi T. I., Roussev I., de Zeeuw D. L., Sokolov I. V., Powell K. G., Tóth G., et al., 2004, *JGRA*, 109, A01102. doi:10.1029/2002JA009672
- Marsch E., Tu C.-Y., 1990, *JGR*, 95, 11945. doi:10.1029/JA095iA08p11945
- Mishra, W. and Wang, Y.: 2018, *The Astrophysical Journal* **865**, 50. doi:10.3847/1538-4357/aadb9b.
- Mishra, W., Doshi, U., and Srivastava, N.: 2021, *Frontiers in Astronomy and Space Sciences* **8**, 142. doi:10.3389/fspas.2021.713999.
- Moldwin, M.B., Ford, S., Lepping, R., Slavin, J., and Szabo, A.: 2000, *Geophys. Res. Lett.* **27**, 57. doi:10.1029/1999GL010724.
- Moore, D.W.: 1959, *Journal of Fluid Mechanics* **6**, 113. doi:10.1017/S0022112059000520.
- Moore, D.W.: 1963, *Journal of Fluid Mechanics* **16**, 161. doi:10.1017/S0022112063000665.
- Nicolaou, G., Livadiotis, G., Wicks, R.T., Verscharen, D., and Maruca, B.A.: 2020, *The Astrophysical Journal* **901**, 26. doi:10.3847/1538-4357/abaaae.
- Nieves-Chinchilla T., Colaninno R., Vourlidas A., Szabo A., Lepping R. P., Boardsen S. A., Anderson B. J., et al., 2012, *JGRA*, 117, A06106. doi:10.1029/2011JA017243
- Nieves-Chinchilla T., Linton M. G., Hidalgo M. A., Vourlidas A., Savani N. P., Szabo A., Farrugia C., et al., 2016, *ApJ*, 823, 27. doi:10.3847/0004-637X/823/1/27
- Nieves-Chinchilla, T., Vourlidas, A., Raymond, J. C., et al. 2018, *Sol. Phys.*, 293, 25
- Nieves-Chinchilla, T., Jian, L.K., Balmaceda, L., Vourlidas, A., dos Santos, L.F.G., and Szabo, A.: 2019, *Solar Physics* **294**, 89. doi:10.1007/s11207-019-1477-8.
- Nieves-Chinchilla, T., Alzate, N., Cremades, H., Rodríguez-García, L., Dos Santos, L.F.G., Narock, A., and, ...: 2022, *The Astrophysical Journal* **930**, 88. doi:10.3847/1538-4357/ac590b.
- Odstrčil D., Pizzo V. J., 1999, *JGR*, 104, 493. doi:10.1029/1998JA900038
- Odstrčil, D. and Pizzo, V.J.: 2009, *Solar Physics* **259**, 297. doi:10.1007/s11207-009-9449-z.
- Parker, E. N. 2009, *Climate and Weather of the Sun-earth System (CAWSES): Selected Papers from the 2007 Kyoto Symposium*, 23
- Richardson, I.G. and Cane, H.V.: 2010, *Solar Physics* **264**, 189. doi:10.1007/s11207-010-9568-6.
- Rollett, T., Möstl, C., Temmer, M., Veronig, A., and Farrugia, C.J.: 2012, *Solar Heliospheric and INterplanetary Environment (SHINE 2012)*.
- Russell, C. T., Shinde, A. A., & Jian, L. 2005, *Advances in Space Research*, 35, 2178
- Sachdeva, N., Subramanian, P., Colaninno, R., & Vourlidas, A. 2015, *ApJ*, 809, 158
- Sachdeva, N., Subramanian, P., Vourlidas, A., & Bothmer, V. 2017, *Sol. Phys.*, 292, 118
- Savani N. P., Owens M. J., Rouillard A. P., Forsyth R. J., Davies J. A., 2010, *ApJL*, 714, L128. doi:10.1088/2041-8205/714/1/L128
- Savani, N.P., Owens, M.J., Rouillard, A.P., Forsyth, R.J., Kusano, K., Shiota, D., and, ...: 2011, *The Astrophysical Journal* **732**, 117. doi:10.1088/0004-637X/732/2/117.
- Scolini, C., Rodriguez, L., Mierla, M., Pomoell, J., and Poedts, S.: 2019, *Astronomy and Astrophysics* **626**, A122. doi:10.1051/0004-6361/201935053.
- Spruit, H.C.: 2013, *arXiv e-prints*, arXiv:1301.5572.
- St. Cyr O. C., Plunkett S. P., Michels D. J., Paswaters S. E., Koomen M. J., Simnett G. M., Thompson B. J., et al., 2000, *JGR*, 105, 18169. doi:10.1029/1999JA000381
- Tóth, G., van der Holst, B., Sokolov, I.V., De Zeeuw, D.L., Gombosi, T.I., Fang, F., and, ...: 2012, *Journal of Computational Physics* **231**, 870. doi:10.1016/j.jcp.2011.02.006.
- Temmer, M.: 2021, *Living Reviews in Solar Physics* **18**, 4. doi:10.1007/s41116-021-00030-3.
- Verbeke C., Schmieder B., Démoulin P., Dasso S., Grison B., Samara E., Scolini C., et al., 2022, *arXiv*, arXiv:2207.03168
- von Steiger, R. and Richardson, J.D.: 2006, *Space Science Reviews* **123**, 111. doi:10.1007/s11214-006-9015-z.
- Vršnak, B. and Gopalswamy, N.: 2002, *Journal of Geophysical Research (Space Physics)* **107**, 1019. doi:10.1029/2001JA000120.
- Vršnak, B., Vrbanec, D., Čalogović, J., et al. 2009, *Universal Heliophysical Processes*, 271
- Vršnak, B., Žic, T., Vrbanec, D., et al. 2013, *Sol. Phys.*, 285, 295
- Wang C., Richardson J. D., 2004, *JGRA*, 109, A06104. doi:10.1029/2004JA010379
- Webb D. F., Howard T. A., Fry C. D., Kuchar T. A., Odstrčil D., Jackson B. V., Bisi M. M., et al., 2009, *SoPh*, 256, 239. doi:10.1007/s11207-009-9351-8
- Weber, E.J. and Davis, L.: 1967, *The Astrophysical Journal* **148**, 217. doi:10.1086/149138.
- Weiss, A., Möstl, C., Nieves-Chinchilla, T., Amerstorfer, T., Palmerio, E., Reiss, M., and, ...: 2020, *EGU General Assembly Conference Abstracts*. doi:10.5194/egusphere-egu2020-8398.
- Xie, H., Ofman, L., and Lawrence, G.: 2004, *Journal of Geophysical Research (Space Physics)* **109**, A03109. doi:10.1029/2003JA010226.

Appendix A: Data Table

Table A.1. The list of the 152 WIND ICME events we use in this study. The arrival date and time of the ICME at the position of WIND measurement and the arrival and departure dates & times of the associated magnetic clouds (MCs) are taken from WIND ICME catalogue (<https://wind.nasa.gov/ICME.index.php>). The 14 events marked with and asterisk (*) coincide with the near earth counterparts of 14 CMEs listed in Sachdeva et al. (2017).

CME event number	CME Arrival date and time[UT] (1AU)	MC start date and time [UT]	MC end date and time [UT]	Flux rope type
1	1995 03 04, 00:36	1995 03 04, 11:23	1995 03 05, 03:06	Fr
2	1995 04 03, 06:43	1995 04 03, 12:45	1995 04 04, 13:25	F+
3	1995 06 30, 09:21	1995 06 30, 14:23	1995 07 02, 16:47	Fr
4	1995 08 22, 12:56	1995 08 22, 22:19	1995 08 23, 18:43	Fr
5	1995 09 26, 15:57	1995 09 27, 03:36	1995 09 27, 21:21	Fr
6	1995 10 18, 10:40	1995 10 18, 19:11	1995 10 20, 02:23	Fr
7	1996 02 15, 15:07	1996 02 15, 15:07	1996 02 16, 08:59	F+
8	1996 04 04, 11:59	1996 04 04, 11:59	1996 04 04, 21:36	Fr
9	1996 05 16, 22:47	1996 05 17, 01:36	1996 05 17, 11:58	F+
10	1996 05 27, 14:45	1996 05 27, 14:45	1996 05 29, 02:22	Fr
11	1996 07 01, 13:05	1996 07 01, 17:16	1996 07 02, 10:17	Fr
12	1996 08 07, 08:23	1996 08 07, 11:59	1996 08 08, 13:12	Fr
13	1996 12 24, 01:26	1996 12 24, 03:07	1996 12 25, 11:44	F+
14	1997 01 10, 00:52	1997 01 10, 04:47	1997 01 11, 03:36	F+
15	1997 04 10, 17:02	1997 04 11, 05:45	1997 04 11, 19:10	Fr
16	1997 04 21, 10:11	1997 04 21, 11:59	1997 04 23, 07:11	F+
17	1997 05 15, 01:15	1997 05 15, 10:00	1997 05 16, 02:37	F+
18	1997 05 26, 09:09	1997 05 26, 15:35	1997 05 28, 00:00	Fr
19	1997 06 08, 15:43	1997 06 09, 06:18	1997 06 09, 23:01	Fr
20	1997 06 19, 00:00	1997 06 19, 05:31	1997 06 20, 22:29	Fr
21	1997 07 15, 03:10	1997 07 15, 06:48	1997 07 16, 11:16	F+
22	1997 08 03, 10:10	1997 08 03, 13:55	1997 08 04, 02:23	Fr
23	1997 08 17, 01:56	1997 08 17, 06:33	1997 08 17, 20:09	Fr
24	1997 09 02, 22:40	1997 09 03, 08:38	1997 09 03, 20:59	Fr
25	1997 09 18, 00:30	1997 09 18, 04:07	1997 09 19, 23:59	F+
26	1997 10 01, 11:45	1997 10 01, 17:08	1997 10 02, 23:15	Fr
27	1997 10 10, 03:08	1997 10 10, 15:33	1997 10 11, 22:00	F+
28	1997 11 06, 22:25	1997 11 07, 06:00	1997 11 08, 22:46	F+
29	1997 11 22, 09:12	1997 11 22, 17:31	1997 11 23, 18:43	F+
30	1997 12 30, 01:13	1997 12 30, 09:35	1997 12 31, 08:51	Fr
31	1998 01 06, 13:29	1998 01 07, 02:23	1998 01 08, 07:54	F+
32	1998 01 28, 16:04	1998 01 29, 13:12	1998 01 31, 00:00	F+
33	1998 03 25, 10:48	1998 03 25, 14:23	1998 03 26, 08:57	Fr
34	1998 03 31, 07:11	1998 03 31, 11:59	1998 04 01, 16:18	Fr
35	1998 05 01, 21:21	1998 05 02, 11:31	1998 05 03, 16:47	Fr
36	1998 06 02, 10:28	1998 06 02, 10:28	1998 06 02, 09:16	Fr
37	1998 06 24, 10:47	1998 06 24, 13:26	1998 06 25, 22:33	F+
38	1998 07 10, 22:36	1998 07 10, 22:36	1998 07 12, 21:34	F+
39	1998 08 19, 18:40	1998 08 20, 08:38	1998 08 21, 20:09	F+
40	1998 10 18, 19:30	1998 10 19, 04:19	1998 10 20, 07:11	F+

Table A.2. continued

CME event number	CME Arrival date and time[UT] (1AU)	MC start date and time [UT]	MC end date and time [UT]	Flux rope type
41	1999 02 11, 17:41	1999 02 11, 17:41	1999 02 12, 03:35	Fr
42	1999 07 02, 00:27	1999 07 03, 08:09	1999 07 05, 13:13	Fr
43	1999 09 21, 18:57	1999 09 21, 18:57	1999 09 22, 11:31	Fr
44	2000 02 11, 23:34	2000 02 12, 12:20	2000 02 13, 00:35	Fr
45	2000 02 20, 21:03	2000 02 21, 14:24	2000 02 22, 13:16	Fr
46	2000 03 01, 01:58	2000 03 01, 03:21	2000 03 02, 03:07	Fr
47	2000 07 01, 07:12	2000 07 01, 07:12	2000 07 02, 03:34	Fr
48	2000 07 11, 22:35	2000 07 11, 22:35	2000 07 13, 04:33	Fr
49	2000 07 28, 06:38	2000 07 28, 14:24	2000 07 29, 10:06	F+
50	2000 09 02, 23:16	2000 09 02, 23:16	2000 09 03, 22:32	Fr
51	2000 10 03, 01:02	2000 10 03, 09:36	2000 10 05, 03:34	F+
52	2000 10 12, 22:33	2000 10 13, 18:24	2000 10 14, 19:12	Fr
53	2000 11 06, 09:30	2000 11 06, 23:05	2000 11 07, 18:05	Fr
54	2000 11 26, 11:43	2000 11 27, 09:30	2000 11 28, 09:36	Fr
55	2001 04 21, 15:29	2001 04 22, 00:28	2001 04 23, 01:11	Fr
56	2001 10 21, 16:39	2001 10 22, 01:17	2001 10 23, 00:47	Fr
57	2001 11 24, 05:51	2001 11 24, 15:47	2001 11 25, 13:17	Fr
58	2001 12 29, 05:16	2001 12 30, 03:24	2001 12 30, 19:10	Fr
59	2002 02 28, 05:06	2002 02 28, 19:11	2002 03 01, 23:15	Fr
60	2002 03 18, 13:14	2002 03 19, 06:14	2002 03 20, 15:36	Fr
61	2002 03 23, 11:24	2002 03 24, 13:11	2002 03 25, 21:36	Fr
62	2002 04 17, 11:01	2002 04 17, 21:36	2002 04 19, 08:22	F+
63	2002 07 17, 15:56	2002 07 18, 13:26	2002 07 19, 09:35	Fr
64	2002 08 18, 18:40	2002 08 19, 19:12	2002 08 21, 13:25	Fr
65	2002 08 26, 11:16	2002 08 26, 14:23	2002 08 27, 10:47	Fr
66	2002 09 30, 07:54	2002 09 30, 22:04	2002 10 01, 20:08	F+
67	2002 12 21, 03:21	2002 12 21, 10:20	2002 12 22, 15:36	Fr
68	2003 01 26, 21:43	2003 01 27, 01:40	2003 01 27, 16:04	Fr
69	2003 02 01, 13:06	2003 02 02, 19:11	2003 02 03, 09:35	Fr
70	2003 03 20, 04:30	2003 03 20, 11:54	2003 03 20, 22:22	Fr
71	2003 06 16, 22:33	2003 06 16, 17:48	2003 06 18, 08:18	Fr
72	2003 08 04, 20:23	2003 08 05, 01:10	2003 08 06, 02:23	Fr
73	2003 11 20, 08:35	2003 11 20, 11:31	2003 11 21, 01:40	Fr
74	2004 04 03, 09:55	2004 04 04, 01:11	2004 04 05, 19:11	F+
75	2004 09 17, 20:52	2004 09 18, 12:28	2004 09 19, 16:58	Fr
76	2005 05 15, 02:10	2005 05 15, 05:31	2005 05 16, 22:47	F+
77	2005 05 20, 04:47	2005 05 20, 09:35	2005 05 22, 02:23	F+
78	2005 07 17, 14:52	2005 07 17, 14:52	2005 07 18, 05:59	Fr
79	2005 10 31, 02:23	2005 10 31, 02:23	2005 10 31, 18:42	Fr
80	2006 02 05, 18:14	2006 02 05, 20:23	2006 02 06, 11:59	F+
81	2006 09 30, 02:52	2006 09 30, 08:23	2006 09 30, 22:03	F+
82	2006 11 18, 07:11	2006 11 18, 07:11	2006 11 20, 04:47	Fr
83	2007 05 21, 22:40	2007 05 21, 22:45	2007 05 22, 13:25	Fr
84	2007 06 08, 05:45	2007 06 08, 05:45	2007 06 09, 05:15	Fr
85	2007 11 19, 17:22	2007 11 20, 00:33	2007 11 20, 11:31	Fr

Table A.3. continued

CME event number	CME Arrival date and time[UT] (1 AU)	MC start date and time [UT]	MC end date and time [UT]	Flux rope type
86	2008 05 23, 01:12	2008 05 23, 01:12	2008 05 23, 10:46	F+
87	2008 09 03, 16:33	2008 09 03, 16:33	2008 09 04, 03:49	F+
88	2008 09 17, 00:43	2008 09 17, 03:57	2008 09 18, 08:09	Fr
89	2008 12 04, 11:59	2008 12 04, 16:47	2008 12 05, 10:47	Fr
90	2008 12 17, 03:35	2008 12 17, 03:35	2008 12 17, 15:35	Fr
91	2009 02 03, 19:21	2009 02 03, 01:12	2009 02 04, 19:40	F+
92	2009 03 11, 22:04	2009 03 12, 01:12	2009 03 13, 01:40	F+
93	2009 04 22, 11:16	2009 04 22, 14:09	2009 04 22, 20:37	Fr
94	2009 06 03, 13:40	2009 06 03, 20:52	2009 06 05, 05:31	Fr
95	2009 06 27, 11:02	2009 06 27, 17:59	2009 06 28, 20:24	F+
96	2009 07 21, 02:53	2009 07 21, 04:48	2009 07 22, 03:36	Fr
97	2009 09 10, 10:19	2009 09 10, 10:19	2009 09 10, 19:26	Fr
98	2009 09 30, 00:44	2009 09 30, 06:59	2009 09 30, 19:11	Fr
99	2009 10 29, 01:26	2009 10 29, 01:26	2009 10 29, 23:45	F+
100	2009 11 14, 10:47	2009 11 14, 10:47	2009 11 15, 11:45	Fr
101	2009 12 12, 04:47	2009 12 12, 19:26	2009 12 14, 04:47	Fr
102	2010 01 01, 22:04	2010 01 02, 00:14	2010 01 03, 09:06	Fr
103	2010 02 07, 18:04	2010 02 07, 19:11	2010 02 09, 05:42	Fr
104*	2010 03 23, 22:29	2010 03 23, 22:23	2010 03 24, 15:36	Fr
105*	2010 04 05, 07:55	2010 04 05, 11:59	2010 04 06, 16:48	Fr
106*	2010 04 11, 12:20	2010 04 11, 21:36	2010 04 12, 14:12	Fr
107	2010 05 28, 01:55	2010 05 29, 19:12	2010 05 29, 17:58	Fr
108*	2010 06 21, 03:35	2010 06 21, 06:28	2010 06 22, 12:43	Fr
109*	2010 09 15, 02:24	2010 09 15, 02:24	2010 09 16, 11:58	Fr
110*	2010 10 31, 02:09	2010 10 30, 05:16	2010 11 01, 20:38	Fr
111	2010 12 19, 00:35	2010 12 19, 22:33	2010 12 20, 22:14	F+
112	2011 01 24, 06:43	2011 01 24, 10:33	2011 01 25, 22:04	F+
113*	2011 03 29, 15:12	2011 03 29, 23:59	2011 04 01, 14:52	Fr
114	2011 05 28, 00:14	2011 05 28, 05:31	2011 05 28, 22:47	F+
115	2011 06 04, 20:06	2011 06 05, 01:12	2011 06 05, 18:13	Fr
116	2011 07 03, 19:12	2011 07 03, 19:12	2011 07 04, 19:12	Fr
117*	2011 09 17, 02:57	2011 09 17, 15:35	2011 09 18, 21:07	Fr
118	2012 02 14, 07:11	2012 02 14, 20:52	2012 02 16, 04:47	Fr
119	2012 04 05, 14:23	2012 04 05, 19:41	2012 04 06, 21:36	Fr
120	2012 05 03, 00:59	2012 05 04, 03:36	2012 05 05, 11:22	Fr
121	2012 05 16, 12:28	2012 05 16, 16:04	2012 05 18, 02:11	Fr
122	2012 06 11, 02:52	2012 06 11, 11:31	2012 06 12, 05:16	Fr
123*	2012 06 16, 09:03	2012 06 16, 22:01	2012 06 17, 11:23	F+
124*	2012 07 14, 17:39	2012 07 15, 06:14	2012 07 17, 03:22	Fr
125	2012 08 12, 12:37	2012 08 12, 19:12	2012 08 13, 05:01	Fr
126	2012 08 18, 03:25	2012 08 18, 19:12	2012 08 19, 08:22	Fr
127*	2012 10 08, 04:12	2012 10 08, 15:50	2012 10 09, 17:17	Fr
128	2012 10 12, 08:09	2012 10 12, 18:09	2012 10 13, 09:14	Fr
129*	2012 10 31, 14:28	2012 10 31, 23:35	2012 11 02, 05:21	F+
130*	2013 03 17, 05:21	2013 03 17, 14:09	2013 03 19, 16:04	Fr

Table A.4. continued

CME event number	CME Arrival date and time[UT] (1 AU)	MC start date and time [UT]	MC end date and time [UT]	Flux rope type
131*	2013 04 13, 22:13	2013 04 14, 17:02	2013 04 17, 05:30	F+
132	2013 04 30, 08:52	2013 04 30, 12:00	2013 05 01, 07:12	Fr
133	2013 05 14, 02:23	2013 05 14, 06:00	2013 05 15, 06:28	Fr
134	2013 06 06, 02:09	2013 06 06, 14:23	2013 06 08, 00:00	F+
135	2013 06 27, 13:51	2013 06 28, 02:23	2013 06 29, 11:59	Fr
136	2013 09 01, 06:14	2013 09 01, 13:55	2013 09 02, 01:56	Fr
137	2013 10 30, 18:14	2013 10 30, 18:14	2013 10 31, 05:30	Fr
138	2013 11 08, 21:07	2013 11 08, 23:59	2013 11 09, 06:14	Fr
139	2013 11 23, 00:14	2013 11 23, 04:47	2013 11 23, 15:35	Fr
140	2013 12 14, 16:47	2013 12 15, 16:47	2013 12 16, 05:30	Fr
141	2013 12 24, 20:36	2013 12 25, 04:47	2013 12 25, 17:59	F+
142	2014 04 05, 09:58	2014 04 05, 22:18	2014 04 07, 14:24	Fr
143	2014 04 11, 06:57	2014 04 11, 06:57	2014 04 12, 20:52	F+
144	2014 04 20, 10:20	2014 04 21, 07:41	2014 04 22, 06:12	Fr
145	2014 04 29, 19:11	2014 04 29, 19:11	2014 04 30, 16:33	Fr
146	2014 06 29, 04:47	2014 06 29, 20:53	2014 06 30, 11:15	Fr
147	2014 08 19, 05:49	2014 08 19, 17:59	2014 08 21, 19:09	F+
148	2014 08 26, 02:40	2014 08 27, 03:07	2014 08 27, 21:49	Fr
149	2015 01 07, 05:38	2015 01 07, 06:28	2015 01 07, 21:07	F+
150	2015 09 07, 13:05	2015 09 07, 23:31	2015 09 09, 14:52	F+
151	2015 10 06, 21:35	2015 10 06, 21:35	2015 10 07, 10:03	Fr
152	2015 12 19, 15:35	2015 12 20, 13:40	2015 12 21, 23:02	Fr

**Appendix B: The List of C_x , C_p and C_r for All The
Events in Our Dataset**

Table B.1. C_x (Equation 9), C_p (Equation 10) and C_r (Equation 12) for all the events in the dataset. The 14 events marked with and asterisk (*) coincide with the near earth counterparts of 14 CMEs listed in Sachdeva et al. (2017).

CME event number	Using BGI			Using BG2		
	C_x	C_p	C_r	C_x	C_p	C_r
1	2.11	6.85	1.78	28.08	6.89	3.34
2	24.93	3.23	0.52	5.71	0.91	2.95
3	6.35	1.82	3.47	7.62	1.42	4.16
4	9.36	2.68	2.29	19.19	6.56	8.23
5	11.35	4.14	7.55	7.09	4.42	2.52
6	69.85	16.07	15.37	42.55	11.20	7.23
7	0.49	1.65	-0.20	5.68	1.80	0.26
8	4.79	1.74	3.22	4.94	1.82	10.74
9	1.16	1.62	0.29	13.06	2.55	18.30
10	7.35	2.63	2.17	13.03	4.78	4.13
11	5.65	2.90	5.80	10.37	7.06	4.82
12	6.53	1.70	2.36	5.08	1.72	4.80
13	8.77	1.96	1.70	7.80	2.34	2.38
14	18.79	4.08	18.01	40.73	8.69	8.38
15	5.62	7.52	7.08	13.68	5.35	1.06
16	3.94	12.08	3.48	15.62	7.96	9.40
17	83.94	24.15	1.88	32.90	7.72	2.01
18	4.69	2.14	24.73	4.06	1.74	4.50
19	37.80	4.98	11.83	22.26	4.01	30.68
20	11.57	3.84	15.12	11.57	3.84	15.12
21	13.06	3.61	9.08	12.89	5.15	4.86
22	7.01	6.34	10.06	34.91	5.75	12.53
23	7.07	1.35	4.12	7.63	1.41	4.87
24	7.87	10.35	9.93	18.73	10.51	2.35
25	4.23	7.82	15.08	7.60	4.65	13.96
26	20.23	2.32	10.74	2.24	0.15	0.30
27	10.62	2.78	35.34	11.12	2.89	30.14
28	21.81	8.47	3.23	15.95	3.71	4.32
29	46.27	8.62	1.95	21.75	5.84	1.66
30	30.85	14.60	4.16	21.60	5.63	7.22
31	34.43	8.88	21.85	17.12	6.18	4.05
32	10.44	1.60	1.57	15.60	2.73	3.71
33	17.38	4.91	1.03	5.52	2.27	4.65
34	1.06	1.06	0.01	0.96	1.10	-0.03
35	8.15	4.37	0.16	3.41	1.18	0.31
36	2.88	3.05	2.15	13.91	3.07	4.65
37	1.97	4.01	1.72	5.76	1.66	1.07
38	40.72	6.69	50.49	16.17	2.24	6.40
39	11.18	3.60	3.26	20.53	6.48	9.92
40	17.51	6.37	6.66	42.52	5.20	14.20

CME event number	Using BGI			Using BG2		
	C_x	C_p	C_r	C_x	C_p	C_r
41	10.79	8.44	7.76	4.74	5.71	1.43
42	29.70	0.82	1.15	17.42	0.67	1.63
43	1.56	3.52	3.96	4.12	2.98	9.42
44	1.94	5.38	2.80	9.30	1.81	1.30
45	38.53	4.29	19.14	23.95	3.40	12.96
46	19.02	2.69	1.07	18.73	2.68	1.20
47	1.18	2.83	0.69	3.79	1.74	1.85
48	5.04	2.35	1.77	3.55	0.23	1.52
49	10.12	4.39	1.01	9.48	5.30	1.04
50	10.11	1.36	0.32	4.08	0.63	0.69
51	17.47	6.91	6.55	10.04	4.95	9.27
52	5.09	2.81	2.33	17.54	3.37	4.06
53	31.83	18.57	3.61	87.69	5.66	14.80
54	8.37	3.36	0.16	7.67	1.71	0.33
55	18.96	6.35	9.46	28.15	8.26	24.59
56	1.77	3.58	0.04	1.68	3.50	0.04
57	189.13	7.05	1.40	177.90	4.06	2.15
58	42.62	5.95	60.55	17.51	4.67	32.86
59	4.05	2.04	1.65	4.75	2.29	1.35
60	133.84	5.51	22.01	93.76	6.20	19.50
61	41.65	3.89	47.33	84.49	5.60	34.64
62	44.67	2.48	3.51	38.32	2.01	3.27
63	116.44	3.04	13.85	49.05	1.29	68.57
64	18.86	0.81	1.25	21.38	1.94	3.73
65	3.16	4.67	1.05	1.44	3.45	0.17
66	17.37	10.03	11.50	5.07	3.36	3.74
67	5.90	1.86	1.95	4.66	1.58	0.57
68	48.21	1.64	0.86	34.78	1.71	1.43
69	6.77	0.85	1.05	9.15	1.76	0.24
70	41.44	1.56	13.90	39.08	1.57	8.93
71	55.44	7.18	9.34	7.72	1.48	5.16
72	7.63	2.71	0.04	4.49	3.29	0.32
73	299.67	35.64	12.01	211.51	38.28	8.27
74	42.12	8.24	27.90	27.12	6.92	9.22
75	2.31	0.88	0.06	1.46	0.65	0.06
76	228.01	19.54	2.54	252.44	21.85	2.32
77	10.97	1.75	1.43	19.42	3.18	5.24
78	23.28	9.95	4.86	11.68	5.32	2.52
79	14.42	6.83	14.05	6.63	3.75	3.17
80	7.29	2.46	5.57	5.97	2.35	8.63
81	44.21	18.40	2.87	15.35	13.98	1.49
82	7.80	1.88	13.10	58.77	2.01	21.42
83	42.13	6.85	0.85	23.76	6.67	3.49
84	23.96	6.14	12.48	7.88	2.81	7.85
85	78.21	18.09	3.95	58.24	12.72	3.60

Table B.2. continued

CME event number	Using BG1			Using BG2		
	C_x	C_p	C_r	C_x	C_p	C_r
86	1.28	1.33	0.36	18.99	1.31	1.76
87	20.65	7.36	0.59	6.09	1.44	0.86
88	21.97	2.14	0.54	22.01	2.17	0.55
89	21.43	5.62	1.03	7.17	0.76	1.26
90	57.20	4.35	61.71	22.71	1.63	34.01
91	29.19	8.97	7.29	15.22	12.15	6.30
92	57.55	11.76	15.98	19.02	9.73	8.38
93	0.97	0.78	-0.03	14.13	1.14	6.47
94	6.72	1.89	10.43	6.07	1.98	7.64
95	33.10	5.15	4.08	25.83	5.18	16.91
96	6.92	10.10	15.12	4.12	1.47	6.78
97	11.24	2.23	1.89	5.50	1.99	18.23
98	10.49	4.64	1.25	14.59	7.01	6.45
99	27.84	4.77	7.78	14.93	3.98	16.30
100	10.48	4.28	3.07	3.28	1.14	2.29
101	1.46	2.77	0.60	3.10	2.57	8.72
102	6.34	6.97	32.60	6.36	2.70	20.34
103	31.52	3.03	3.42	16.72	1.49	9.87
104*	5.15	2.46	2.26	4.14	1.86	4.52
105*	3.47	1.65	1.09	36.34	1.73	1.87
106	23.62	8.48	4.92	13.53	7.17	4.01
107	33.93	10.58	9.87	61.34	12.83	17.35
108*	8.41	0.55	0.63	18.10	2.63	12.23
109*	2.37	4.20	2.52	3.67	0.81	2.84
110*	2.31	5.31	0.60	10.17	2.49	6.58
111	21.07	2.83	0.56	14.96	2.90	4.01
112	8.28	2.65	0.38	6.80	2.51	6.06
113*	7.09	6.40	33.30	62.10	6.70	175.26
114	16.49	3.59	0.86	11.06	1.29	1.73
115	6.90	11.13	1.70	28.72	11.68	0.80
116	16.61	1.60	11.74	12.66	1.26	16.99
117*	66.65	3.93	24.50	59.62	4.27	17.83
118	17.09	3.08	10.92	6.30	0.98	7.28
119	2.25	3.47	10.35	2.99	1.69	9.29
120	7.82	1.81	6.17	6.61	1.83	3.14
121	3.01	6.54	2.01	17.14	2.84	10.32
122	95.55	4.59	0.56	31.61	3.10	24.51
123*	8.68	56.12	5.93	84.04	60.46	2.50
124	314.97	20.82	8.30	220.67	13.09	6.22
125	14.69	3.44	5.16	14.44	3.35	4.52
126	1.98	4.34	0.89	25.11	9.73	4.38
127*	27.89	4.23	10.20	17.13	3.38	8.68
128	63.11	3.40	18.11	57.82	2.83	13.88
129*	8.10	8.64	8.01	17.45	4.46	4.86
130*	35.51	2.26	3.64	39.95	2.62	3.29

CME event number	Using BGI			Using BG2		
	C_x	C_p	C_r	C_x	C_p	C_r
131*	3.88	1.92	4.45	45.50	2.71	21.16
132	2.64	9.18	0.68	6.94	2.07	4.54
133	10.42	4.57	0.80	3.57	1.68	3.15
134	60.52	7.87	3.75	60.83	8.14	4.25
135	70.57	11.85	6.38	60.93	10.70	30.87
136	26.59	1.30	1.46	11.22	0.47	2.26
137	3.24	4.63	2.49	4.56	1.05	5.80
138	2.72	6.16	0.94	11.38	6.84	4.85
139	19.44	3.57	6.46	17.86	4.86	4.74
140	167.01	6.27	2.72	17.32	0.33	4.11
141	24.61	7.93	8.90	18.73	6.53	9.87
142	12.24	4.65	2.51	17.41	5.81	1.91
143	1.68	4.68	1.88	13.04	4.24	5.25
144	2.58	2.19	0.02	0.84	0.72	-0.05
145	11.09	5.61	1.37	8.38	5.30	6.93
146	9.25	4.18	7.89	3.90	1.55	3.03
147	69.95	12.32	54.23	17.57	4.58	8.12
148	16.97	7.82	8.60	18.11	14.99	6.20
149	8.60	2.94	1.68	4.33	2.82	2.16
150	11.09	5.12	6.40	7.57	2.83	4.65
151	6.06	8.26	1.38	3.61	6.24	2.08
152	10.81	5.11	2.08	12.09	9.06	5.98

Table B.4. continued